PHYSICAL REVIEW E **109**, 014221 (2024)

Hebbian and anti-Hebbian adaptation-induced dynamical states in adaptive networks

S. Thamizharasan,[1] V. K. Chandrasekar,[2,*] M. Senthilvelan,[1] and D. V. Senthilkumar[3,†]
[1]*Department of Nonlinear Dynamics, School of Physics, Bharathidasan University, Tiruchirappalli-620 024, Tamil Nadu, India*
[2]*Centre for Nonlinear Science & Engineering, Department of Physics, School of Electrical & Electronics Engineering, SASTRA Deemed University, Thanjavur-613 401, Tamil Nadu, India*
[3]*School of Physics, Indian Institute of Science Education and Research, Thiruvananthapuram-695 551, Kerala, India*

(Received 29 April 2023; accepted 13 December 2023; published 19 January 2024)

We investigate the interplay of an external forcing and an adaptive network, whose connection weights coevolve with the dynamical states of the phase oscillators. In particular, we consider the Hebbian and anti-Hebbian adaptation mechanisms for the evolution of the connection weights. The Hebbian adaptation manifests several interesting partially synchronized states, such as phase and frequency clusters, bump state, bump frequency phase clusters, and forced entrained clusters, in addition to the completely synchronized and forced entrained states. Anti-Hebbian adaptation facilitates the manifestation of the itinerant chimera characterized by randomly evolving coherent and incoherent domains along with some of the aforementioned dynamical states induced by the Hebbian adaptation. We introduce three distinct measures for the strength of incoherence based on the local standard deviations of the time-averaged frequency and the instantaneous phase of each oscillator, and the time-averaged mean frequency for each bin to corroborate the distinct dynamical states and to demarcate the two parameter phase diagrams. We also arrive at the existence and stability conditions for the forced entrained state using the linear stability analysis, which is found to be consistent with the simulation results.

DOI: 10.1103/PhysRevE.109.014221

I. INTRODUCTION

Adaptive networks are an important class of complex networks that constitute the framework for self-adapting smart systems. Generally, adaptive networks that have been extensively investigated in the literature are the ones that self-adapt their structure in congruence with their dynamical states. It is also to be noted that adaptation may also alter the nodal dynamics, as in the case of frequency adaptation of applauding audiences and fireflies [1]. However, a simultaneous adaptation of both network structure and nodal dynamics is pivotal in several complex networks that underlie the mechanism behind their intriguing collective dynamical states (cf. [2]). Note that nodal dynamics refers to the dynamics of the individual units constituting the networks, while network dynamics refers to structural changes of the network. Adaptive networks have been employed widely in neurological systems [3] including biological [4], chemical [5], epidemic [4], social systems [4,6], etc. In particular, in adaptive networks, where the coupling coevolves with the dynamical state, the adaptation rate is much slower than the intrinsic timescale of the employed dynamical system, so that the overall dynamics may be analyzed using the singular perturbation theory [7].

Adaptive networks have been at the heart of recent investigations that have reported several exotic self-organizing dynamical states that are exclusive to the nature of the adaptability of the networks [7]. In particular, multifrequency clusters [8], splay states, antipodal states, double antipodal clusters [9], and several other mesoscale structures [10,11] are found to be specific to the adaptive networks. Very recently, two distinct first-order phase transitions to synchronization were reported due to the tradeoff between the nodal heterogeneity and the adaptivity of the network of phase oscillators [12]. Specifically, it has been shown that the nature of the defects in the frequency distribution determines an abrupt single-step transition or a more gradual multistep transition to full synchronization [12]. Two distinct types of itinerant chimera were shown in adaptively coupled phase oscillators with an external forcing [13]. Recent studies on the adaptive coupling with simplicial complexes elucidated the emergence of an abrupt desynchronization transition [14,15] and abrupt anti-phase-synchronization [16,17].

Adaptation rules that have been employed in most of the aforementioned investigations involve the spike time-dependent plasticity, Hebbian, and anti-Hebbian rules. Hebb [18] postulated that the synaptic strength increases (decreases) based on the in-phase (out-of-phase) firing of the neurons, later verified by experiments [3,19], which was referred to as the Hebbian (anti-Hebbian) learning rule in the literature. Neurophysiological experiments revealed that the evolution of the synaptic coupling is governed by the presynaptic and postsynaptic spike timings [20]. Such a spike time-dependent synaptic plasticity has been encoded in the evolution equation for the coupling weights that depend on the relative timing of the phase oscillators to reveal several interesting dynamical states [8–13,21–34].

The role of adaptive coupling in multiplex networks [9], the interplay between the adaptive coupling and the simplicial

---

[*] chandru25nld@gmail.com

[†] skumar@iisertvm.ac.in

complexes [14,16], and that between adaptivity and nodal heterogeneity [12] have been studied recently. In particular, a framework that provides insight into the spectral structure of a multiplex network has been developed using multiplex decomposition [9], and a mean-field approach has been shown to successfully capture the nature of multicluster order parameters governed by the Hebbian adaptation [14]. Very recently, a mean-field approach has been developed to describe the dynamics of multicluster states and their role in determining the nature of the phase transitions in finite-size adaptive networks [12]. Nevertheless, the response of the coevolving connection weights and the phases of the complex networks to an external forcing, equivalent to the cognitive task in neural networks, is rather poorly understood. A recent investigation revealed a host of exotic collective states in an adaptive network subjected to an external periodic forcing [13], which has essentially adapted spike time dependent plasticity as the adaptive mechanism. External perturbations in terms of periodic forcing are very natural in real-world systems. Examples include resonances [35–38], event-related desynchronization [39], circadian rhythms [40–42], etc.

In this work, we consider an adaptive network whose connection weights coevolve along with the dynamical states of the phase oscillator in accordance with the Hebbian and anti-Hebbian adaptive rules [12,21], which is subjected to an external sinusoidal forcing [13]. We unravel the collective dynamical states due to a delicate balance between adaptive rules and external forcing. In particular, the Hebbian rule facilitates the manifestation of several interesting partially and completely synchronized states, such as two-clusters, multiclusters, frequency-clusters, bump state, bump frequency clusters, and forced entrained clusters, including a completely synchronized state and a forced entrained state. The anti-Hebbian rule facilitates the emergence of itinerant chimera, incoherent states, multiclusters states, and forced entrained states. Further, we introduce three distinct measures for the strength of incoherence to corroborate the distinct dynamical states and to demarcate the two parameter phase diagrams along with the Kuramoto order parameters. We also arrive at the existence and stability conditions for the forced entrained state, which is found to match very well with the simulation boundary of the forced entrained state. In a nutshell, the tradeoff between the Hebbian and anti-Hebbian adaptive rules with the external forcing results in a gallery of exotic nontrivial collective dynamical states.

The structure of the paper is as follows. In Sec. II, we discuss the model of globally coupled Kuramoto oscillators with suitable adaptation rules for their connection weights. In Sec. III, we unravel the distinct intriguing dynamical states facilitated by the Hebbian adaptation mechanism, we introduce the three distinct measures for the strength of incoherence, and we discuss the dynamical transitions in one- and two-parameter phase diagrams. We elucidate the dynamical states induced by the anti-Hebbian adaptation rule for the evolution of the connection weights along with the one- and two-parameter phase diagrams depicting the dynamical transitions in Sec. IV. We also elucidate the dynamical transitions as a function of the parameter that governs the distinct adaptation rules in Sec. V. Finally, we provide a summary and discussion in Sec. VI.

II. MODEL

Our model comprises a network of globally coupled identical phase oscillators acted upon by an external periodic force, whose evolution equation is represented by

$$\dot{\theta}_i = \lambda - \frac{1}{N}\sum_{j=1}^{N} k_{ij}\sin(\theta_i - \theta_j + \alpha) + f\sin\theta_i, \qquad (1)$$

$$i = 1, 2, 3, \ldots, N,$$

$$\dot{k}_{ij} = \varepsilon\sin(\theta_i - \theta_j + \beta), \quad |k_{ij}| \leqslant 1, \qquad (2)$$

where λ is the natural frequency of the oscillators, k_{ij} is the coupling weight from the jth to ith oscillator, θ_i is the phase of the ith oscillator of the network, f is the strength of the external sinusoidal forcing, α is the phase lag parameter, ε signifies the timescale separation between the fast oscillator dynamics and the slower adaptation rule, and the parameter β governs the distinct adaptation rules, namely the spike time-dependent plasticity, the Hebbian rule, and the anti-Hebbian rule [21]. In particular, when $\beta = 0$, the evolution equation for the coupling weights in Eq. (1) mimics the spike time-dependent plasticity. The evolution equation for the coupling weights mimics the Hebbian and anti-Hebbian rules for $\beta = \pi/2$ and $-\pi/2$, respectively. Note that the constraint in Eq. (2) is enforced by setting $k_{ij} = 1$ for $k_{ij} > 1$ and $k_{ij} = -1$ for $k_{ij} < -1$ as the connection weight cannot grow indefinitely. The boundedness of the connection weight can also be implemented by imposing a soft limitation using a nonlinear term, which was also confirmed to result in qualitatively the same results as that of the hard constraint employed in Eq. (2) [21].

It should also be noted that we have employed the phase oscillators even though the aforementioned adaptation rules originally stem from the interneuronal dynamics as the phase variables are known to play the role of relative spike timings of any weakly coupled nonlinear oscillators near Hopf bifurcation [43,44]. Deduction of phase models from weakly coupled nonlinear oscillators and their investigations have been extensively used to model networks of neurons [45], ecological systems [46], etc. Note that the phase variables are time coarse-grained variables similar to the experimentally measured phases [47], and consequently the phase description of such coupled nonlinear oscillators is proved to explain the experimentally observed facts qualitatively [48]. The phase models also allow for an analytical description of the observed macroscopic dynamical states. In the absence of external forcing, only two cluster states, a coherent state and a chaotic state are identified depending on the nature of the evolution of the coupling weights as determined by β [21]. In the chaotic state, the relative phases between the oscillators and the coupling weights are chaotically shuffled. In addition, self-assembled multiclusters can be shown to be designed by controlling the weight dynamics. Further, synchronization was found to be completely inhibited in the absence of any specific adaptation rule for the coupling weights when the latter are fixed and strongly anticorrelated for $f = 0$ [49]. Nevertheless, simulation results suggested that the finite-size effect causes the oscillators to be entrained in synchronized frequency clusters close to the synchronization transition. The anti-Hebbian adaptation rule in single-layer networks [28], and the Hebbian

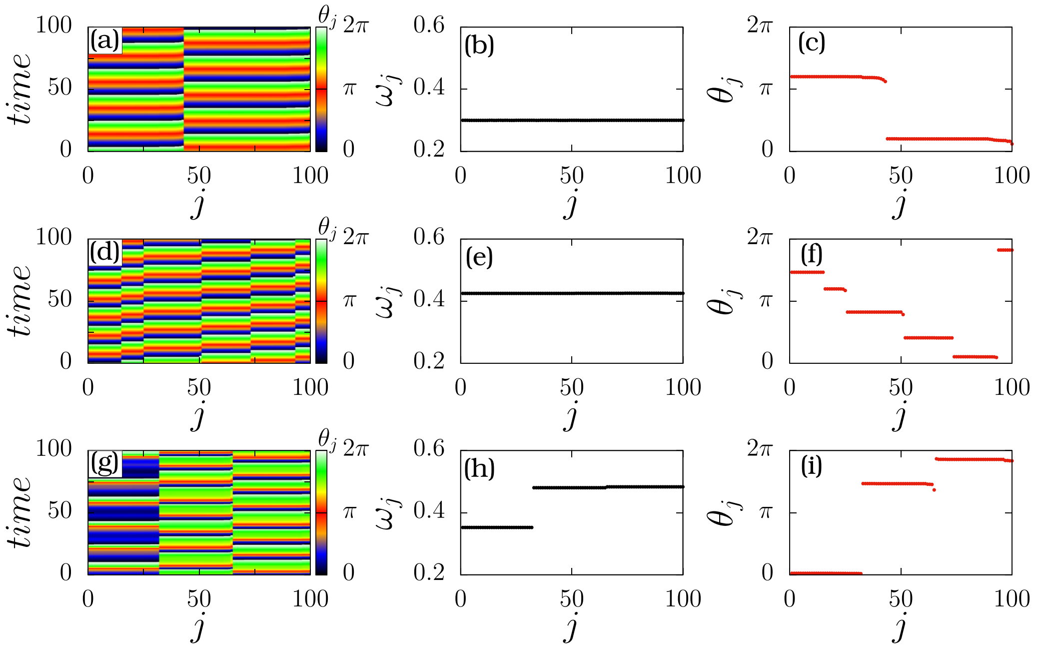

FIG. 1. The left column depicts the time evolution of the phases, while the middle and right columns depict the corresponding time-averaged mean frequencies and the snapshot of the instantaneous phases, respectively. [(a)–(c)] Two-cluster state (TC) for $\alpha = 0.78$ and $f = 0$, [(d)–(f)] Multicluster state (MC) for $\alpha = 1.10$ and $f = 0.08$, and [(g)–(i)] frequency cluster state (FC) for $\alpha = 0.63$ and $f = 0.56$. The observed dynamical states are also marked in the two-parameter phase diagram in Fig. 6 at their respective parameter values.

adaptation rule in multiplex networks [50], were shown to facilitate explosive synchronization, abrupt desynchronization in pure simplicial complexes [14], and an abrupt transition to anti-phase-clustering in pairwise and triad (two simplexes) coupling [16] in the absence of external forcing.

In the following, we will consider both the Hebbian and anti-Hebbian adaptive mechanisms to unravel the emergent dynamical states due to the interplay between the coevolving coupling weights and the phases, and the external sinusoidal forcing.

III. HEBBIAN ADAPTATION RULE

A. Dynamical states

The initial conditions for the phases of the oscillators θ_i are uniformly distributed in the interval $[0, 2\pi)$, whereas the initial conditions for the connection weights k_{ij} are uniformly distributed in the interval $(-1, 1)$, $\forall j$. We have fixed the timescale parameter as $\varepsilon = 0.005$, the natural frequency of the oscillators as $\lambda = 1$, and the number of oscillators $N = 100$ throughout the manuscript. We use a Runge-Kutta fourth-order integration scheme to integrate the evolution equations in Eq. (1) with a step size of 0.01. Three distinct collective dynamical states that emerge as the response of the coevolving connection weights and the phases for the external periodic forcing are depicted in Fig. 1 for three distinct values of the phase lag parameter α and the strength of the external force f. The space-time plot, the time-averaged mean frequencies, and the snapshot of the instantaneous phases are depicted, respectively, in the left, middle, and right columns of Fig. 1. The two-cluster state (TC) is depicted in the first row of Fig. 1 for $\alpha = 0.78$ and $f = 0$. The time evolution of the phases of the oscillators [see Fig. 1(a)] clearly illustrates the two-cluster states, whereas the corresponding time-averaged mean frequencies of the oscillators are entrained [see Fig. 1(b)] elucidating that the two-cluster state is purely a phase cluster. Further, the snapshot of the instantaneous phases in Fig. 1(c) also confirms the two-cluster state of the state variables. Multiphase clusters (MC) are evident in the middle row of Fig. 1 for $\alpha = 1.10$ and $f = 0.08$. The space-time plot in Fig. 1(d) and the snapshot of the instantaneous phases in Fig. 1(f) elucidates the multiphase cluster state as corroborated by the entrained time-averaged mean frequencies of the oscillators illustrated in Fig. 1(e). Finally, the last row in Fig. 1 for $\alpha = 0.63$ and $f = 0.56$ displays the frequency cluster state (FC). In particular, it is a three-frequency-cluster state as corroborated by Figs. 1(g)–1(i).

The interplay between the external force and the coevolving connection weights and the phases of the oscillators also manifests bump state, bump frequency two-phase clusters, and bump frequency three-phase clusters as depicted in Fig. 1. The space-time plot, the time-averaged mean frequencies, and the snapshot of the instantaneous phases are depicted, respectively, in the left, middle, and right columns in Fig. 2. The phase oscillators are partially inactive and partially active, as is evident from the space-time plot in Fig. 2(a) and in the snapshot of the instantaneous phases in Fig. 2(c) for $\alpha = 1.54$ and $f = 0.4$. The active and inactive nature of the phase oscillators are also corroborated by the time-averaged mean frequencies of the oscillators depicted in Fig. 2(b). Such a coexisting coherent quiescent state and incoherent active state has recently been identified as a bump state (BS) [13,51–53]. In contrast, two clusters are observed in the space-time plot in Fig. 2(d) for $\alpha = 0.78$ and $f = 1.5$. The snapshot of the instantaneous phases in Fig. 2(f) illustrates nearly two phase clusters, however the time-averaged mean

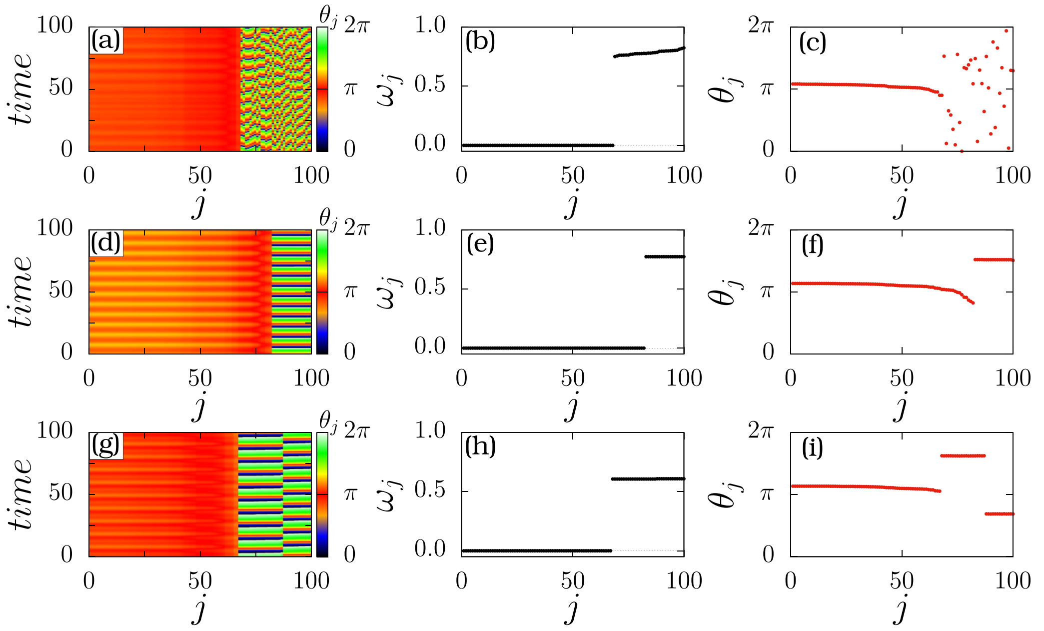

FIG. 2. The left column depicts the time evolution of the phases, while the middle and right columns depict the corresponding time=averaged mean frequencies and the snapshot of the instantaneous phases, respectively. [(a)–(c)] Bump state (BS) for $\alpha = 1.54$ and $f = 0.4$, [(d)–(f)] bump frequency two phase clusters state (BF2PC) for $\alpha = 0.78$ and $f = 1.5$, and [(g)–(i)] bump frequency three phase clusters state (BF3PC) for $\alpha = 1.1$ and $f = 0.54$. The observed dynamical states are also marked in the two-parameter phase diagram in Fig. 6 at their respective parameter values.

frequencies of the oscillators in Fig. 2(e) corroborate that one among the phase clusters is characterized by nearly zero mean frequency, whereas the other cluster with a finite mean frequency is attributed to the bump frequency with two phase clusters (BF2PC). Analogously, bump frequency with three phase clusters (BF3PC) state is depicted in Figs. 2(g)–1(i) for $\alpha = 1.1$ and $f = 0.54$.

Three more distinct self-organizing behaviors due to the tradeoff between the external forcing and the adaptive coupling weights are observed in the (α, f) parameter space. The space-time plot, the time-averaged mean frequencies, and the snapshot of the instantaneous phases are depicted, respectively, in the left, middle, and right columns in Fig. 3. The phases of all the oscillators are completely entrained for $\alpha = 0.16$ and $f = 0.79$, resulting in the synchronized (SYN) state as depicted in Figs. 3(a)–3(c). The forced entrained state (FE), where all the oscillators are entrained to the frequency of the external forcing, is shown in the middle row of Fig. 3 [see Figs. 3(d)–3(f)] for $\alpha = 1.10$ and $f = 1.52$. The forced entrained state with phase clusters (FEC) for $\alpha = 1.10$ and $f = 1.05$ is depicted in Figs. 3(g)–3(i), where the oscillators are entrained to the frequency of the external forcing but grouped as two phase clusters [see Fig. 3(i)].

B. Strength of incoherence

We define three distinct measures for the strength of incoherence [54] based on the local standard deviations of the time-averaged frequency, the instantaneous phase, and the mean of time-averaged frequencies of the oscillators to distinguish the distinct collective dynamical states and to demarcate the corresponding regions in the (α, f) parameter space. To this aim, N oscillators are divided into M bins of equal size $n = N/M$ [55]. The local standard deviation (σ_m) of the frequency of each oscillator in each bin is estimated using

$$\sigma_m = \sqrt{\frac{1}{n}\sum_{j=n(m-1)+1}^{mn}[\omega_j - \bar{\omega}_m]^2},$$
$$m = 1, 2, \dots, M. \qquad (3)$$

with $\bar{\omega}_m = \frac{1}{n}\sum_{j=n(m-1)+1}^{mn}\omega_j$. Here, ω_j corresponds to the time-averaged frequency of the jth oscillator. Now, the strength of incoherence S calculated using the local standard deviation (σ_m) of the frequency of each oscillator is defined as [54]

$$S = 1 - \frac{\sum_{m=1}^{M} s_m}{M}, \quad s_m = \Theta(\delta - \sigma_m), \qquad (4)$$

where Θ is the Heaviside step function and δ is a predefined threshold, which is fixed as $\delta = 0.005$ throughout the manuscript for the estimation of S. For all the frequency entrained states, the local standard deviation $\sigma_m = 0$ and consequently $s_m = 1$ for all the bins. Therefore, the strength of incoherence $S = 0$ for the frequency entrained states. In contrast, for the completely incoherent state $\sigma_m > \delta$ and consequently $s_m = 0$ for all the bins, which results in $S = 1$ for the incoherent states. However, for frequency clusters and bump frequency clusters, there is a discontinuous jump of the time-averaged frequency only in the bins are comprised of oscillators from two distinct clusters and hence $s_m = 0$ only in those bins as $\sigma_m > \delta$, while the other bins are characterized by $s_m = 1$. As a consequence, the strength of incoherence $S = N_{fc}/M \neq 0$, where N_{fc} is the number of frequency clusters. Note that S depends on the value of M. Nevertheless, S takes a finite value between 0 and 1 for the bump state, which is

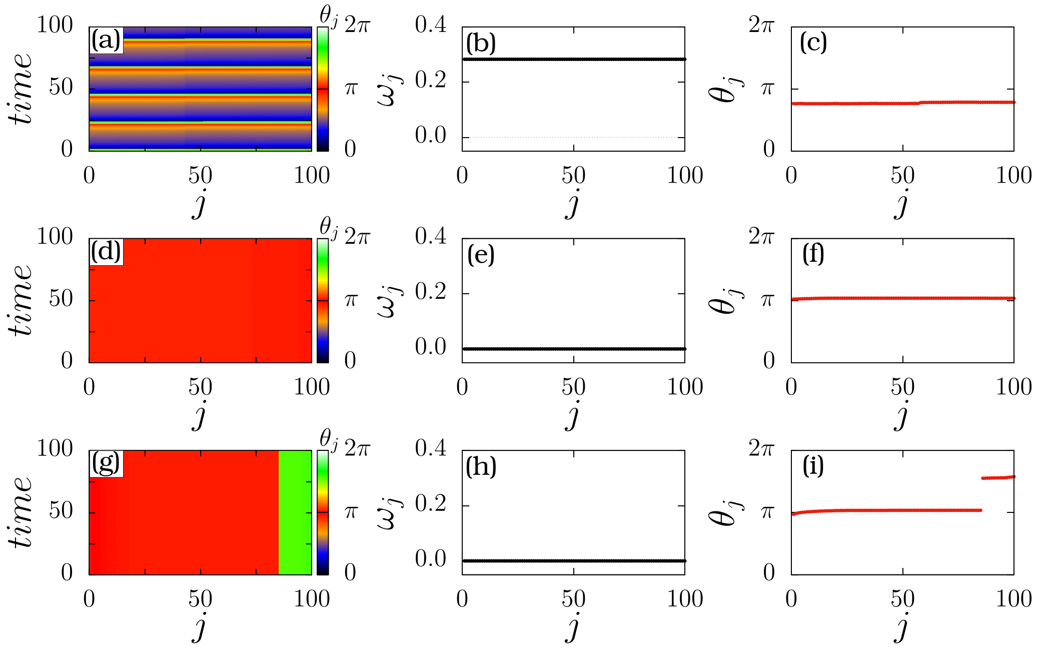

FIG. 3. The left column depicts the time evolution of the phases, while the middle and right columns depict the corresponding time-averaged mean frequencies and the snapshot of the instantaneous phases, respectively. [(a)–(c)] Synchronization (SYN) for $\alpha = 0.16$ and $f = 0.79$, [(d)–(f)] forced entrained state (FE) for $\alpha = 1.10$ and $f = 1.52$, and [(g)–(i)] forced entrained cluster state (FEC) for $\alpha = 1.10$ and $f = 1.05$. The observed dynamical states are also marked in the two-parameter phase diagram in Fig. 6 at their respective parameter values.

characterized by an appreciable number of inactive oscillators and consequently an appreciable number of bins with $s_m = 0$.

Note that the strength of incoherence $S = 1$ for the incoherent state, $0 < S < 1$ for the bump state, and $0 < S << 1$ for frequency clusters and bump frequency clusters, whereas $S = 0$ for the frequency entrained states such as the two-cluster state, multicluster state, synchronized state, forced entrained state, and forced entrained cluster state reported in Figs. 1–3. Hence, S is incapable of distinguishing these states. However, the local standard deviation of the instantaneous phases defined as

$$\hat{\sigma}_m = \sqrt{\frac{1}{n}\sum_{j=n(m-1)+1}^{mn}[\theta_j - \bar{\theta}_m]^2}, \quad m = 1, 2, \ldots, M \tag{5}$$

can be used to distinguish the phase clusters. Here, $\bar{\theta}_m = \frac{1}{n}\sum_{j=n(m-1)+1}^{mn}\theta_j$, where θ_j is the instantaneous phase of the jth oscillator. Now, the strength of incoherence S_σ calculated using the local standard deviation ($\hat{\sigma}_m$) of the instantaneous phase of each oscillator is defined as

$$S_\sigma = 1 - \frac{\sum_{m=1}^{M}\bar{s}_m}{M}, \quad \bar{s}_m = \Theta(\delta - \hat{\sigma}_m). \tag{6}$$

The strength of incoherence $S_\sigma = N_{\mathrm{pc}}/M \neq 0$, where N_{pc} is the number of phase clusters and hence the two-phase clusters and the forced entrained cluster state are characterized by $S_\sigma \neq 0$ but $S_\sigma \ll 1$. Note that we have used $\delta = 0.05$ for the estimation of S_σ throughout the manuscript unless otherwise specified. However, for the multiphase cluster state such as the multiclusters, the bump frequency two-phase clusters, and the bump frequency three-phase clusters, $0 < S_\sigma < 1$. Note that for both the synchronized and the forced entrained states, $S = S_\sigma = 0$.

A much finer distinction of SYN, FE, FC, BF2PC, and BF3PC states can be made using the mean of the time-averaged frequencies in each bin as the majority of the oscillators comprising these states are characterized by the zero mean of the time-averaged frequencies. Hence, we define the strength of incoherence S_ω as

$$S_\omega = 1 - \frac{\sum_{m=1}^{M}\hat{s}_m}{M}, \quad \hat{s}_m = \Theta(\delta - \bar{\omega}_m), \tag{7}$$

where $\bar{\omega}_m$ is the mean of the time-averaged frequencies in the mth bin. Here, we have used $\delta = 0.005$ for the estimation of S_ω throughout the manuscript. For the forced entrained state $\hat{s}_m = 1$ as $\bar{\omega}_m = 0 < \delta$ for all m bins and hence $S_\omega = 0$. Thus, the FE state is characterized by $S = S_\sigma = S_\omega = 0$. $\hat{s}_m = 0$ as $\bar{\omega}_m > \delta$ for the synchronized state, and hence it is characterized by $S_\omega = 1$ and $S = S_\sigma = 0$. Analogously, TC, MC, and FC are characterized by $S_\omega = 1$, whose $\omega_j \neq 0 > \delta$. The bump state and the bump frequency clusters are characterized by $0 < S_\omega < 1$ as there will be a finite number of bins with $\bar{\omega} = 0$ and a finite number of bins with $\bar{\omega} > \delta$.

We have also employed the Kuramoto order parameter [56,57]

$$R_l = \left|\frac{1}{N}\sum_{j=1}^{N} e^{il\theta_j}\right|, \quad l = 1, 2 \tag{8}$$

to corroborate the dynamical states. $R_1 = 1$ characterizes the completely synchronized state, whereas $R_2 = 1$ characterizes the two-cluster state. For the incoherent state both $R_1 = R_2 \approx 0$. The values of the order parameters and the strength of incoherence characterizing distinct dynamical

TABLE I. Characterization of the observed dynamical states using the time-averaged Kuramoto order parameters ($\langle R_1\rangle$ and $\langle R_2\rangle$) and the three distinct measures of the strength of incoherence ($S,\ S_\omega$, and S_σ).

Dynamical states	$\langle R_1\rangle$ and $\langle R_2\rangle$	S	S_ω	S_σ
Two-cluster state (TC)	$\langle R_1\rangle \approx 0 \langle R_2\rangle = 1$	$S = 0$	$S_\omega = 1$	$0 < S_\sigma < 1$
Multiphase cluster (MC)	$0 < \langle R_1\rangle < 1\ 0 < \langle R_2\rangle < 1$	$S = 0$	$S_\omega = 1$	$0 < S_\sigma < 1$
Frequency cluster (FC)	$0 < \langle R_1\rangle < 10 < \langle R_2\rangle < 1$	$0 < S < 1$	$S_\omega = 1$	$0 < S_\sigma < 1$
Bump state (BS)	$0 < \langle R_1\rangle < 10 < \langle R_2\rangle < 1$	$0 < S < 1$	$0 < S_\omega < 1$	$0 < S_\sigma < 1$
Bump frequency with two phase clusters (BF2PC)	$0 < \langle R_1\rangle \leqslant 10 < \langle R_2\rangle \leqslant 1$	$0 < S < 1$	$0 < S_\omega < 1$	$0 < S_\sigma < 1$
Bump frequency with three phase clusters (BF3PC)	$0 < \langle R_1\rangle \leqslant 10 < \langle R_2\rangle \leqslant 1$	$0 < S < 1$	$0 < S_\omega < 1$	$0 < S_\sigma < 1$
Synchronized state (SYN)	$\langle R_1\rangle = \langle R_2\rangle = 1$	$S = 0$	$S_\omega = 1$	$S_\sigma = 0$
Forced entrained state (FE)	$\langle R_1\rangle = \langle R_2\rangle = 1$	$S = 0$	$S_\omega = 0$	$S_\sigma = 0$
Forced entrained state with phase clusters (FEC)	$0 < \langle R_1\rangle < 10 < \langle R_2\rangle < 1$	$S = 0$	$S_\omega = 0$	$0 < S_\sigma < 1$
Incoherent state (ICS)	$\langle R_1\rangle \approx 0 \langle R_2\rangle \approx 0$	$S = 1$	$S_\omega = 1$	$S_\sigma = 1$
Itinerant chimera (IC)	$0 < \langle R_1\rangle < 10 < \langle R_2\rangle < 1$	$S = 1$	$S_\omega = 1$	$S_\sigma = 1$

states are tabulated in Table I. Using these quantification measures to corroborate the observed dynamical states, we will discuss the dynamical transition in one- and two-parameter phase diagrams in the next section.

C. Dynamical transitions in the phase diagrams

The time-averaged Kuramoto order parameters ($\langle R_1\rangle$ and $\langle R_2\rangle$) along with the three distinct strengths of incoherence S, S_ω, and S_σ are used to characterize the dynamical transitions as a function of the strength of the external forcing for three different values of the phase lag parameter $\alpha = 0.16,\ 1.1$, and 1.54 in Figs. 4 and 5, to cover the dynamical transitions among the observed intriguing states. In addition, the time-averaged mean frequency and the instantaneous phase of all the oscillators are also depicted in these figures. The values of the aforementioned set of parameters that corroborate the distinct dynamical states are tabulated in Table I. For $\alpha = 0.16$ [see Fig. 4(a)], the TC state exists in the range of $f \in (0, 0.66)$. There is a transition from TC to FC as f is increased further. FC persists in the range of $f \in (0.66, 0.76)$, which then emerges as a SYN state in the range of $f \in (0.76, 0.83)$.

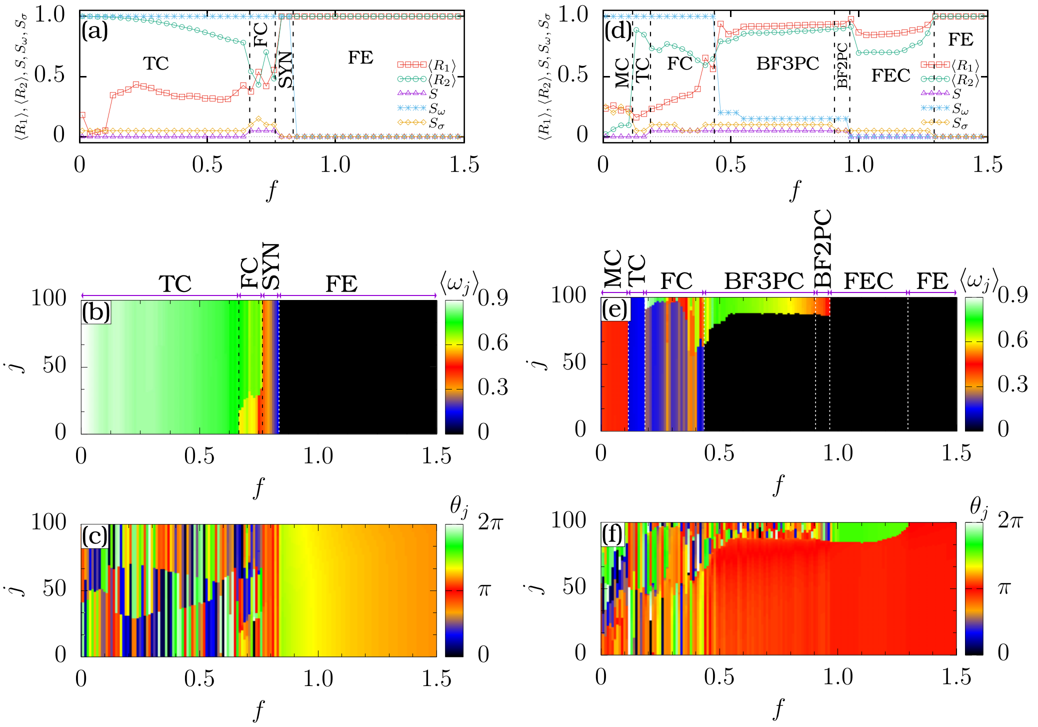

FIG. 4. Dynamical transitions as a function of the external forcing strength f for $\alpha = 0.16$ (left column) and $\alpha = 1.1$ (right column). (a) and (d) The time-averaged order parameters ($\langle R_1\rangle$ and $\langle R_2\rangle$) and the three distinct measures of the strength of incoherence ($S,\ S_\omega$, and S_σ) corroborate the dynamical transition, (b) and (e) time-averaged mean frequency of all the oscillators, and (c) and (f) instantaneous phase of the oscillators. The ranges of f represented as TC, FC, SYN, FE, MC, BF2PC, BF3PC, FEC, and BS correspond to two-cluster state, frequency cluster state, synchronized state, forced entrained state, multicluster state, bump frequency two-phase cluster state, bump frequency three-phase cluster state, forced entrained cluster, and bump state, respectively.

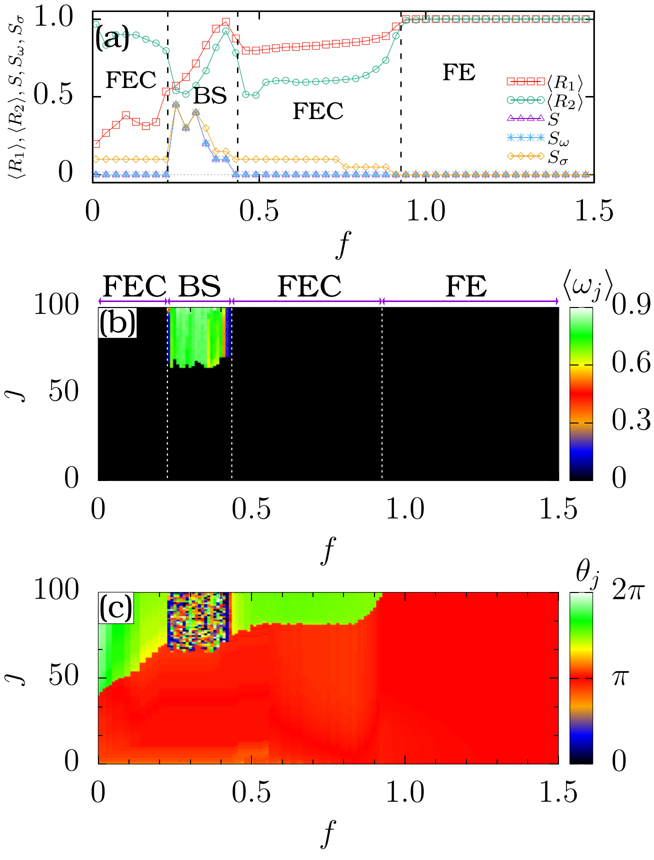

FIG. 5. Dynamical transitions as a function of the external forcing strength f for $\alpha = 1.54$. (a) The time-averaged order parameters ($\langle R_1\rangle$ and $\langle R_2\rangle$) and the three distinct measures of the strength of incoherence (S, S_ω, and S_σ) corroborate the dynamical transition, (b) time-averaged mean frequency of all the oscillators, and (c) instantaneous phase of the oscillators.

Further increase in the strength of the external forcing leads to the FE state in the range of $f \in (0.83, 1.5)$. These dynamical transitions in the respective ranges of f are also clearly visible from the time-averaged mean frequency [see Fig. 4(b)] and the instantaneous phase [see Fig. 4(c)] of the oscillators.

The dynamical transitions observed for $\alpha = 1.1$ are depicted in Figs. 4(d)–4(f). MC exists in the range of $f \in (0, 0.11)$, which then transits to FC via TC as a function of f. TC is stable in the range of $f \in (0.11, 0.18)$ and FC is stabilized in the range of $f \in (0.18, 0.43)$. Further increase in the strength of the forcing results in BF3PC in the range of $f \in (0.43, 0.9)$, which then manifests as BF2PC in a rather narrow range of $f \in (0.9, 0.96)$. BF2PC leads to the manifestation of the FEC state in the range of $f \in (0.96, 1.29)$. There is a transition from FEC to FE state for $f \geqslant 1.29$ in the explored range of f. The observed dynamical transitions in the respective ranges of f are also clearly visible from the time-averaged mean frequency [see Fig. 4(e)] and the instantaneous phase [see Fig. 4(f)] of the oscillators. The FEC state reemerges via BS as a function of f for $\alpha = 1.54$ [see Figs. 5(a)–5(c)]. FEC exists in the ranges of $f \in (0, 0.22)$ and $f \in (0.43, 0.92)$, while BS is stable in the range of $f \in (0.22, 0.43)$. Finally, the FE state emerges from the FEC state as the strength of the forcing is increased further in the range of $f \in (0.92, 1.5)$.

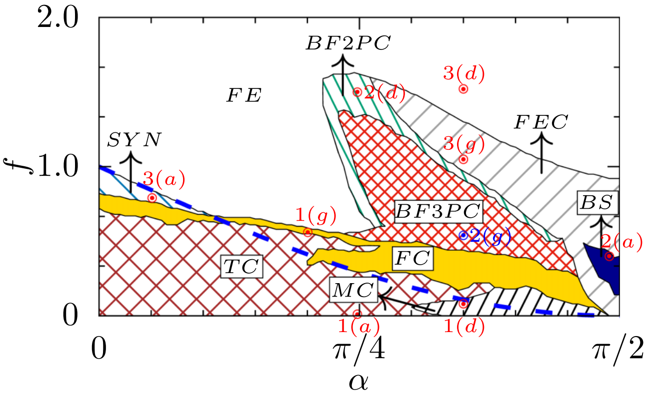

FIG. 6. The two-parameter phase diagram in the (α, f) parametric space. Abbreviations representing the distinct dynamical states are the same as in Fig. 4. The initial conditions for θ_i and k_{ij} are uniformly distributed in the interval $[0, 2\pi)$ and $(-1, 1)\ \forall\ j$, respectively. The blue dashed line corresponds to the analytical critical curve corresponding to the forced entrained state, above which the latter is stable. The parameter values of the dynamical states depicted in Figs. 1–3 are marked in the two-parameter space with their respective figure numbers.

Now, the dynamical transitions observed in Fig. 4 are extended to the (α, f) parametric space by more smoothly varying the phase lag parameter $\alpha \in (0, \pi/2)$ as depicted in Fig. 6. The initial conditions for θ_i and k_{ij} are uniformly distributed in the interval $(0, 2\pi)$ and $(-1, 1)\ \forall\ j$, respectively. There is a transition from TC to FEC via MC, and FC as a function of α in the range of $f \in (0, 0.15)$. Transition from TC to BS via FC and FEC is also observed as a function of α in the range of $f \in (0.15, 0.49)$. For a further increase in f, one can observe the transition from TC to FEC via FC, BF3PC, and BF2PC. In a narrow range of f, FC leads to the stabilization of FE and the latter subsequently leads to BF2PC→BF3PC→BF2PC→FEC as a function of α. Similar dynamical transitions are also seeded from the SYN state in the range of $f \in (0.82, 1)$. For $f \geqslant 1$, FE prevails in a rather large region of the phase diagram. In the range of $f \in (1, 1.63)$, FE reemerges via BF2PC, BF3PC, and FEC as α is increased from the null value. For $f \geqslant 1.63$, only FE is stable in the entire explored range of the phase lag parameter. The stability condition for the FE state can be deduced as follows.

In the FE state, all the oscillators are entrained and hence their phases $\theta_i = \theta^*$ can be obtained as

$$\theta^* = \sin^{-1}\left(\frac{\sum_j k_{ij}\sin(\alpha) - N\lambda}{Nf}\right). \tag{9}$$

The above expression for θ^* admits two solutions only if the coupling weights satisfy the following two conditions: (i) $\frac{1}{N}\sum_{j=1}^{N} k_{ij} = \eta$ should be independent of the oscillator index i and (ii) $|\eta\sin(\alpha)/N - \lambda| \leqslant f$. With $\sin^{-1} : [-1, 1] \rightarrow [-\pi/2, \pi/2]$, the two solutions are given by $\theta_1^* = \theta^*$ and $\theta_2^* = \pi - \theta^*$. Using the linear stability analysis, one can deduce the stability of the fixed points $\theta_{1,2}^*$. The diagonal elements (DF_{ii}) of the stability determining Jacobian J can be obtained as

$$DF_{ii} = \left(\frac{k_{ii}}{N} - \eta\right)\cos\alpha + f\cos(\theta_i^*).$$

The off-diagonal entries (DF_{ij}) of J are

$$DF_{ij} = \frac{k_{ij}}{N}\cos\alpha.$$

The stability determining the characteristic equation corresponding to the Jacobian J can be obtained as

$$[\mu + \eta\cos\alpha - f\cos(\theta^*)]^N = 0,$$

which results in the following N-degenerate eigenvalues:

$$\mu_k = -\eta\cos\alpha \pm f\sqrt{1 - \left(\frac{\eta\sin\alpha - \lambda}{f}\right)^2}$$

for $k = 0, \dots, N-1$. Note that "+" and "−" correspond to the solutions θ_1^* and θ_2^*, respectively. A fold bifurcation leads to the emergence of the FE state at

$$\sqrt{(\eta\cos\alpha)^2 + (\eta\sin\alpha - \lambda)^2} = \pm f. \tag{10}$$

Note that for the Hebbian adaptation rule, the time evolution of k_{ij} becomes

$$\dot{k}_{ij} = \varepsilon \tag{11}$$

$\forall\, i, j$ and the asymptotic ($t \to \infty$) solution of k_{ij} is $k_{ij} = 1$, so that $\eta = 1$. Therefore, the stability condition corresponding to the forced entrained state reduces to

$$\sqrt{1 + \lambda^2 - 2\lambda\sin\alpha} \leqslant f, \tag{12}$$

and the existence condition becomes $|\sin(\alpha) - \lambda| \leqslant f$. The dashed blue line in Fig. 6 corresponds to the existence condition for the FE state, above which the latter is stable. Note that the existence condition turns out to be the stability condition for the Hebbian adaption rule. The analytical critical curve matches with the simulation results for small values of the phase lag parameter (see Fig. 6) for the employed initial conditions. However, the former matches with the latter in a large range of α for a different set of initial conditions for the connection weights (see Fig. 7), where k_{ij} are uniformly distributed in the interval $(-1, 1)\ \forall\, i$. The dynamical transitions in Fig. 7 are almost similar to that observed in Fig. 6 except that the dynamical states observed for large (α, f) parameter space in the latter are squeezed to large values of α and small values of f. We have also confirmed that the two-parameter phase diagram in the (α, f) parametric space for the frequencies $\lambda = 0.5$ and 0.75 are similar to that observed in Figs. 6 and 7 except for the change in the spread of the observed dynamical states elucidating the robustness of the observed states.

We have also distributed cluster initial conditions for both the phases and the connection weights to elucidate the emergent dynamical states. In particular, the cluster initial conditions for θ_i are chosen as 0 for the first 50 oscillators and π for the remaining 50 oscillators, whereas the initial conditions for k_{ij} are fixed as -1 for the intergroup and 1 for the intragroup. The employed cluster initial conditions resulted only in TC, FEC, and FE states as illustrated in Fig. 8. We have superimposed all three phase diagrams in the (α, f) parameter space to elucidate the existence of multistability among the observed dynamical states as depicted in Fig. 9. Note that we have used a specific initial condition in all three two-parameter phase diagrams (Figs. 6–8) in the (α, f) parameter space, and hence their respective phase diagrams have resulted in only monostable dynamical states. Nevertheless, adiabatic initial conditions in both forward and backward traces will certainly elucidate the multistable states as observed in Fig. 9. It is also worthwhile to emphasize that the underlying reason for the emergence of the multistable states is due to the higher-order phase transitions as reported by Omel'chenko *et al.* [58]. However, note that such a transition in Ref. [58] is due to the heterogeneity, whereas in this case it is due to the adaptive nature of the network.

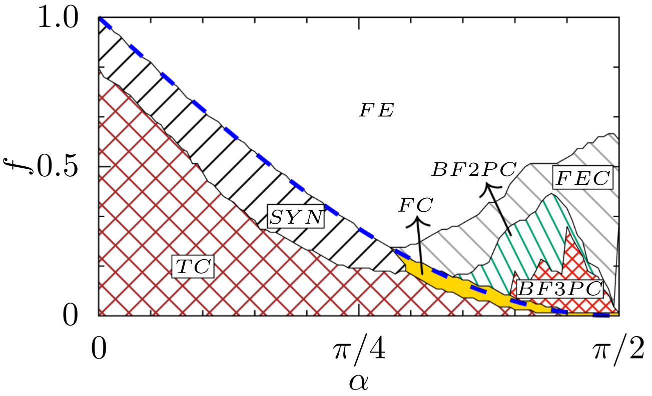

FIG. 7. Same as in Fig. 6 except for a different set of initial conditions for the connection weights, where k_{ij} are uniformly distributed in the interval $(-1, 1)\ \forall\, i$. Note that the initial conditions corresponding to the connection weights of all the j oscillators connected to any given ith oscillator are uniformly distributed in the interval $(-1, 1)$.

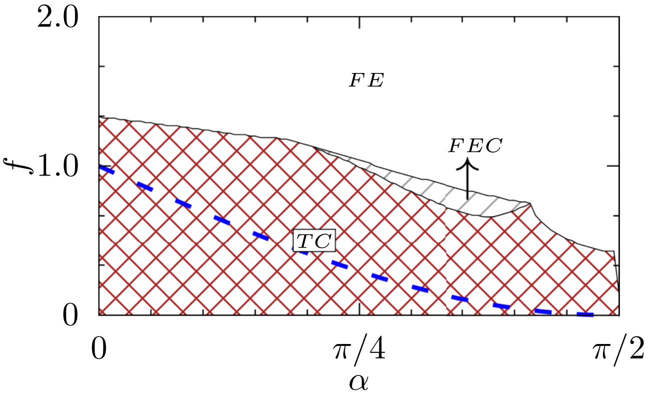

FIG. 8. The two-parameter phase diagram in the (α, f) parametric space for a cluster of initial conditions. The initial conditions for θ_i are chosen as 0 for the first 50 oscillators and π for the remaining 50 oscillators, while the initial conditions for k_{ij} are fixed as -1 for the intergroup and 1 for the intragroup. The other details as the same as in Fig. 6.

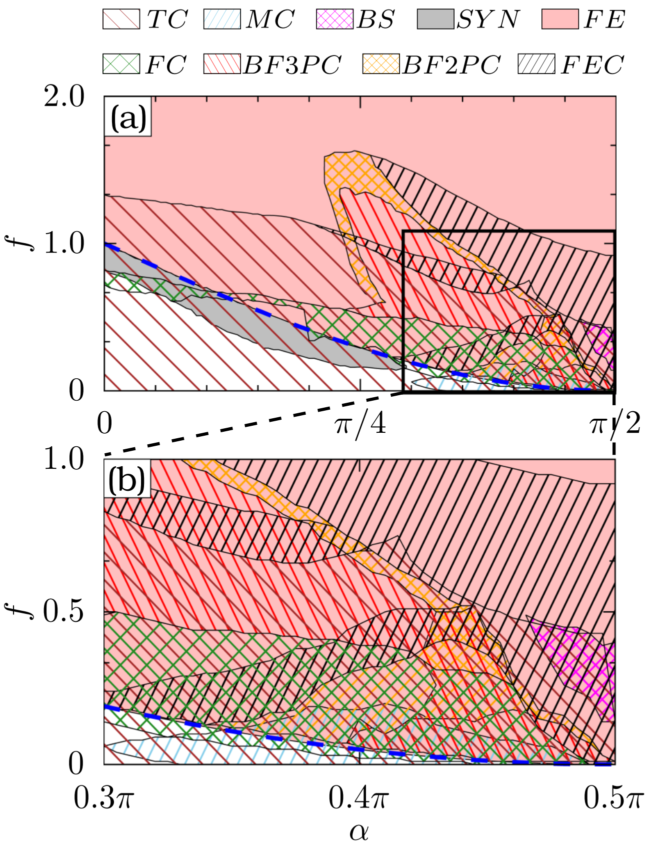

FIG. 9. (a) The two-parameter phase diagram in the (α, f) parametric space for the three different initial conditions employed in Figs. 6–8 depicting multistability among the observed dynamical states. The other details are the same as in Fig. 6. It is evident that Fig. 9(b) is the blown up part of the right lower corner, indicated by a square frame, of Fig. 9 for better visibility of the multistable states.

IV. ANTI-HEBBIAN ADAPTATION RULE

A. Dynamical states

In this section, we choose $\beta = -\pi/2$, which corresponds to the anti-Hebbian adaptation rule for the evolution of the connection weights that coevolve with the phases of the oscillators. The initial conditions for the phases of the oscillators θ_i are uniformly distributed in the interval $[0, 2\pi)$, whereas that of the connection weights k_{ij} are uniformly distributed in the interval $(-1, 1)$, $\forall\, j$. The value of the timescale parameter ε, the natural frequency of the oscillators ω, and the number of phase oscillators are the same as in Sec. III A. Four distinct collective dynamical states that emerge as the response of the coevolving connection weights and the phases for the external periodic forcing are depicted in Fig. 10 for four distinct values of the phase lag parameter α and the strength of the external force f. The space-time plot, the time-averaged mean frequencies, and the snapshot of the instantaneous phases are depicted, respectively, in the left, middle, and right columns of Fig. 10.

The random evolution of the phases of the oscillators and the random instantaneous phases in Figs. 10(a) and 10(c), respectively, elucidate the incoherent state (ICS) for $\alpha = 0.78$ and $f = 0.1$. The time-averaged mean frequencies of all oscillators are also distributed in a range of ω as is evident from Fig. 10(b). The anti-Hebbian adaptation rule has resulted in the fascinating itinerant chimera (IC) [13,59] for $\alpha = 0.78$ and $f = 1.05$, which is characterized by the time-dependent coherent and incoherent domains as depicted in Fig. 10(d). The snapshot of the instantaneous phases [see Fig. 10(e)] of the oscillators also elucidates the coexisting coherent and incoherent domains corroborating the itinerant chimera, whereas the oscillator frequencies are distributed in a range of ω as shown in Fig. 10(f). Note that the main difference between the ICS and IC states is that all the evolution of the oscillators is completely uncorrelated in the ICS state, whereas in the IC state one can observe synchronized epochs of random size coexisting with asynchronous oscillators as the system evolves. For instance, one can observe finite synchronized epochs of random size in Fig. 10(f). The multicluster state is evident from the third row of Fig. 10 for $\alpha = 0.78$ and $f = 1.7$. The space-time plot [see Fig. 10(g)] and the snapshot of the instantaneous phases [see Fig. 10(i)] confirm the multiphase cluster state, while the oscillator frequencies are almost entrained as shown in Fig. 10(h). The forced entrained state is depicted in Figs. 10(j)–10(l) for $\alpha = 0.78$ and $f = 1.9$.

The Kuramoto order parameter R_1 for the incoherent state and the itinerant chimera is depicted in Figs. 11(a) and 11(b), respectively. R_1 has acquired a rather low value near zero for the incoherent state for $\alpha = 0.78$ and $f = 0.1$, whereas the fluctuating R_1 about 0.5 for $\alpha = 0.78$ and $f = 1.05$ is attributed to the fact that there exists a finite degree of coherence and incoherence among the oscillators at any given time t, a characteristic of the itinerant chimera.

B. Dynamical transitions in the phase diagrams

The time-averaged Kuramoto order parameters ($\langle R_1\rangle$ and $\langle R_2\rangle$) along with the three distinct measures of the strength of incoherence (S, S_ω, and S_σ) are used to characterize the dynamical transitions as a function of the strength of the external forcing for the phase lag parameter $\alpha = 0.78$ in Figs. 12(a)–12(c). As discussed above, the Kuramoto order parameters acquire values between $0 < R_{1,2} < 1$ for the IC state. Further, it is also evident from the time-averaged mean frequencies and the snapshot of the instantaneous phases of the itinerant chimera in Figs. 10(e) and 10(f), respectively, that the standard deviations $\sigma_m > \delta$ and $\hat{\sigma}_m > \delta$. Consequently, $s_m = \bar{s}_m = 0$ resulting in $S = S_\sigma = 1$ characterizing the itinerant chimera. Analogously, $\hat{s}_m = 0$ leading to $S_\omega = 1$. The values of the aforementioned set of quantification measures that corroborate the distinct dynamical states are tabulated in Table I. These dynamical transitions in the respective ranges of f are also clearly visible from the time-averaged mean frequency [see Fig. 12(b)] and the instantaneous phase [see Fig. 12(c)] of the oscillators. As characterized by the order parameters and the three distinct strength of incoherence measures, there is a transition from the incoherent state to the forced entrained state via the itinerant chimera and the multicluster state as a function of the phase lag parameter (see Fig. 12).

The dynamical transitions presented in Fig. 12 are extended to the (α, f) parametric space by more smoothly varying the phase lag parameter $\alpha \in (0, \pi/2)$ as depicted in

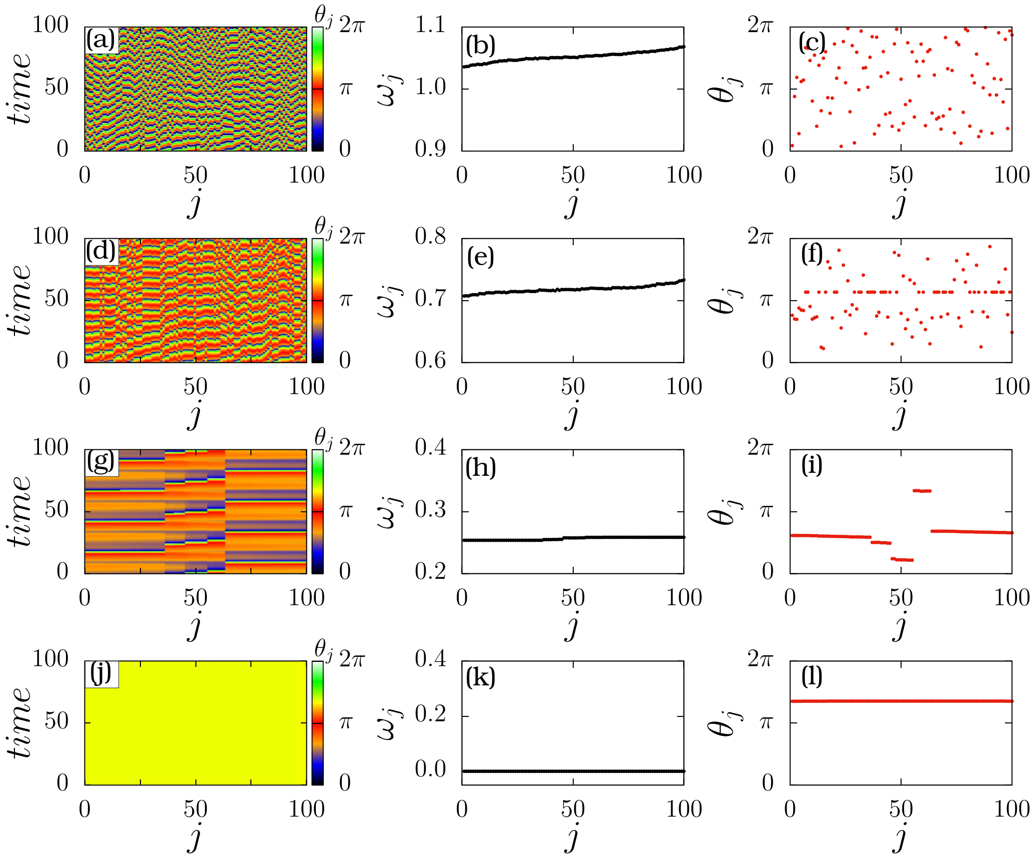

FIG. 10. The left column depicts the time evolution of the phases, while the middle and right columns depict the corresponding time-averaged mean frequencies and the snapshot of the instantaneous phases, respectively. [(a)–(c)] Incoherent state (ICS) for $\alpha = 0.78$ and $f = 0.1$, [(d)–(f)] itinerant chimera (IC) for $\alpha = 0.78$ and $f = 1.05$, [(g)–(i)] multicluster state (MC) for $\alpha = 0.78$ and $f = 1.7$, and [(j)–(l)] forced entrained state for $\alpha = 0.78$ and $f = 1.9$. The observed dynamics states are also marked in the two-parameter phase diagram in Fig. 13 at their respective parameter values.

Fig. 13. The initial conditions for θ_i and k_{ij} are uniformly distributed in the interval $(0, 2\pi)$ and $(-1, 1)\ \forall j$, respectively. There is a transition from ICS→IC→MC→FE as a function of the strength of the external forcing f in almost the entire explored range of the phase lag parameter α. Note that the spread of the itinerant chimera (IC), and multicluster state (MC) increases, whereas that of the forced entrained state decreases as a function of f as $\alpha \to \pi/2$. However, above a critical α (near $\alpha = \pi/2$), the spread of the IC state drastically decreases with an increase in the spread of the MC state. The stability condition for the FE state can be deduced exactly following the procedure adapted for the Hebbian adaptation rule in Sec. III C. Now, the time evolution of k_{ij} for the anti-Hebbian adaptation turns out to be

$$\dot{k}_{ij} = -\varepsilon \tag{13}$$

and the asymptotic ($t \to \infty$) solution of k_{ij} is $k_{ij} = -1$, so $\eta = -1$. Hence, the stability condition corresponding to the forced entrained state reduces to

$$\sqrt{1 + \lambda^2 + 2\lambda \sin\alpha} \leqslant f, \tag{14}$$

while the existence condition becomes $|\sin(\alpha) + \lambda| \leqslant f$. The above analytical stability condition (14) for the FE state is depicted as the blue dashed line in Fig. 13, which almost coincides with the simulation boundary of the FE state at large values of the phase lag parameter α.

The two parameter phase diagram in the (α, f) parametric space is depicted in Fig. 14 for a different set of initial conditions for the connection weights k_{ij} that are uniformly distributed in the interval $(-1, 1)\ \forall\, i$. The dynamical transitions are exactly similar to those observed in Fig. 13. The dashed blue line is the analytical stability condition (14) for the FE state. We have also confirmed that the two-parameter phase diagram in the (α, f) parametric space for the frequencies $\lambda = 0.5$ and 0.75 are similar to that observed in Figs. 13 and 14 except for the change in the spread of the observed

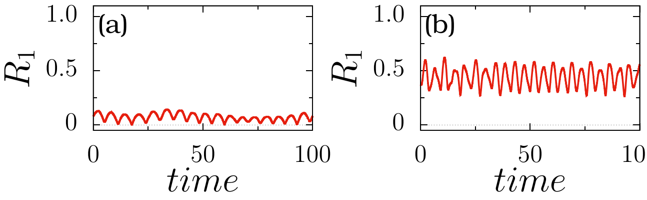

FIG. 11. Order parameter. (a) Incoherent state (ICS) for $\alpha = 0.78$ and $f = 0.1$ and (b) itinerant chimera (IC) $\alpha = 0.78$ and $f = 1.05$.

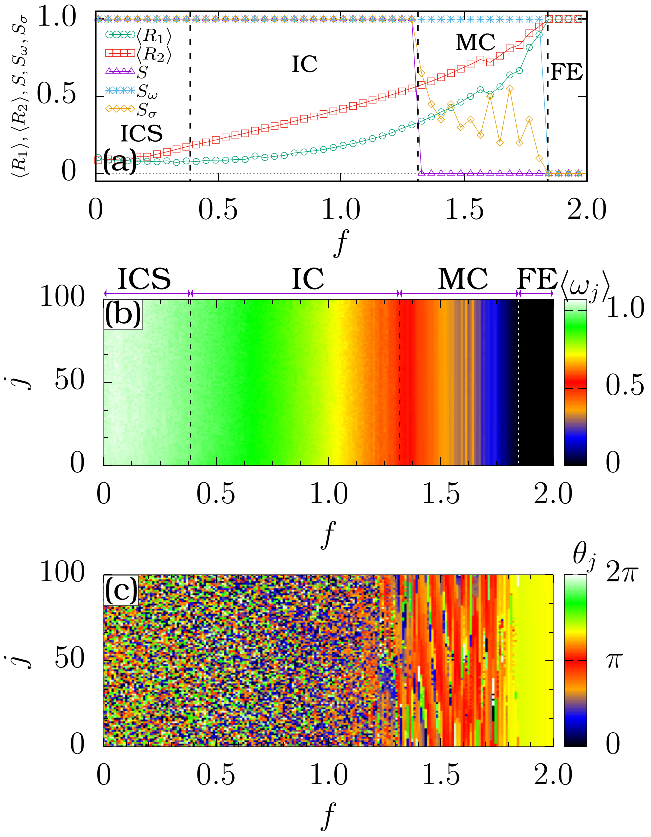

FIG. 12. Dynamical transitions as a function of the external forcing strength f for $\alpha = 0.78$. (a) The time-averaged order parameters ($\langle R_1\rangle$ and $\langle R_2\rangle$) and the three distinct measures of the strength of incoherence (S, S_ω, and S_σ) corroborate the dynamical transition; (b) time-averaged mean frequency of all the oscillators; and (c) instantaneous phase of the oscillators. There is a dynamical transition from the incoherent state (ICS) to a forced entrained state (FE) via itinerant chimera (IC) and multicluster state (MC) as a function f.

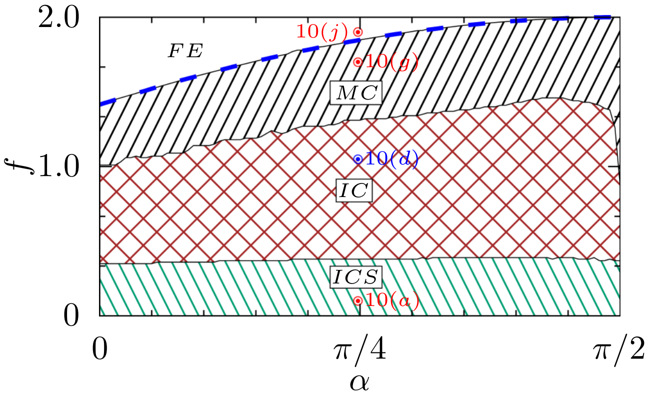

FIG. 13. The two-parameter phase diagram in the (α, f) parametric space. Abbreviations representing the distinct dynamical states are the same as in Fig. 12. The initial conditions for θ_i and k_{ij} are uniformly distributed in the interval $[0, 2\pi)$ and $(-1, 1)\ \forall j$, respectively. The blue dashed line corresponds to the analytical critical curve corresponding to the forced entrained state, above which the latter is stable. The parameter values of the dynamical states depicted in Fig. 10 are marked in the two-parameter space with their respective figure numbers.

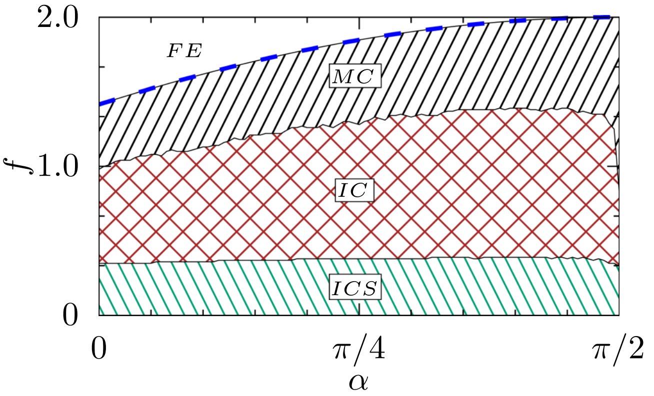

FIG. 14. Same as in Fig. 13 but for a different set of initial conditions for the connection weights, where k_{ij} are uniformly distributed in the interval $(-1, 1)\ \forall\ i$.

dynamical states elucidating the robustness of the observed states. For the cluster initial conditions θ_i are chosen as 0 for the first 50 oscillators and π for the remaining 50 oscillators, whereas the initial conditions for k_{ij} are fixed as -1 for the intergroup and 1 for the intragroup, in which case only MC and FE states are found to be stable (see Fig. 15). Transition from the MC state to the FE state is observed as a function of f in almost the entire explored range of α. We have also superimposed all three phase diagrams in the (α, f) parameter space to elucidate the existence of multistability among the observed dynamical states as depicted in Fig. 16.

V. PHASE DIAGRAMS AS A FUNCTION OF β

In this section, we will elucidate the dynamical transitions in (β, f) parametric space for completeness. The two-parameter phase diagram in the (β, f) parametric space for the phase-lag parameter $\alpha = 0$, and $\pi/4$ is depicted in Figs. 17(a) and 17(b), respectively. The shaded regions marked as TC, FC, SYN, FE, BF2PC, BF3PC, CHI, ICS, IC, FEC, and BS correspond to the two-cluster state, frequency cluster state, synchronized state, forced entrained state, multi-

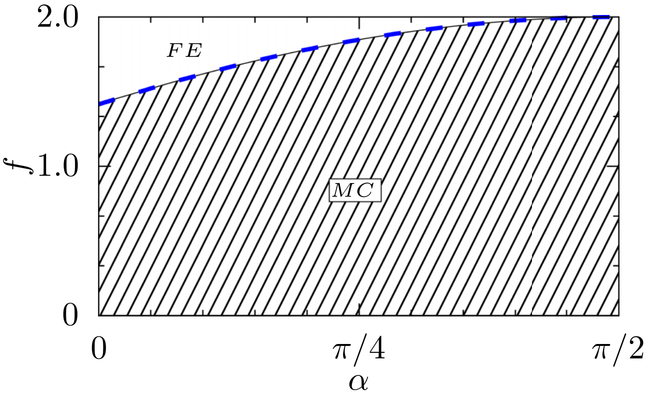

FIG. 15. The two-parameter phase diagram in the (α, f) parametric space for a cluster of initial conditions. The initial conditions for θ_i are fixed as 0 for the first 50 oscillators and π for the remaining 50 oscillators, while the initial conditions for k_{ij} are fixed as -1 for the intergroup and 1 for the intragroup. Other details are the same as in Fig. 13.

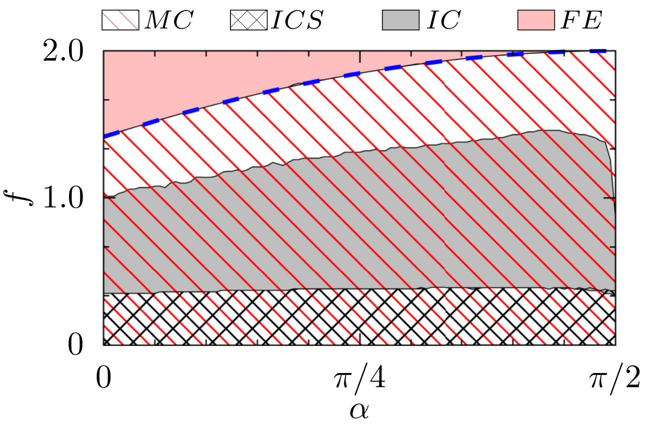

FIG. 16. The two-parameter phase diagram in the (α, f) parametric space for the three different initial conditions employed in Figs. 13–15 depicting multistability among the observed dynamical states. Other details are the same as in Fig. 13.

cluster state, bump frequency two-phase clusters state, bump frequency three-phase cluster state, chimera state, incoherent state, itinerant chimera state, forced entrained cluster, and bump state, respectively. All these states depicted in Fig. 17 are discussed either in Sec. III dealing with the Hebbian adaption rule, or in Sec. IV discussing the effect of the anti-Hebbian adaption rule except for the chimera (CHI) state. Note that the chimera state has been observed only near $\beta = 0$ in Fig. 17(b) for small values of f and in a slightly extended region of the parameter space near $\beta = 0$ for a large f. This is the case of the spike-time-dependent plasticity rule studied exclusively in [13] for $\beta = 0$.

For $\alpha = 0$, there is a transition from ICS to FE state via IC and MC states as a function of f for $\beta < 0$ [see Fig. 17(a)] as observed in Fig. 14 for the case of the anti-Hebbian adaptation rule. For $\beta > 0$, there is a transition from TC to FE via FC and FEC as a function of f in the range of $\beta \in (0, 1)$. Further, one can also observe a transition from TC to FE via FC, and SYN in the range of $\beta \in (1.16, 2.45)$. However for $\beta > 2.45$, there is a direct transition from TC to FE via SYN. One can also observe the transition TC→IC→BS→BF2PC→FE around $\beta = 0$. For $\alpha = \pi/4$, the transition MC→BF3PC→BS→BF2PC is observed in the range of $\beta \in (-\pi, -2.83)$ [see Fig. 17(b)]. Further, there is a transition from ICS to FE state via IC and MC states in the range of $\beta \in (-2.39, -0.91)$ as observed for $\beta < 0$ in Fig. 17(a). The transition TC→FC→BF3PC→BF2PC→FE is observed as a function of f in the range of $\beta \in (0.09, 1.41)$. There is also a transition from MC to FE state via BF3PC, BS, and BF2PC states in the range of $\beta \in (2.58, \pi)$. Similar dynamical transitions are observed in Fig. 6 near $\alpha = \pi/4$. Note that this section essentially encapsulates the results observed in the case of the Hebbian and anti-Hebbian adaption rules in Secs. III and IV, respectively.

VI. CONCLUSION

We have considered an adaptive network of globally coupled Kuramoto oscillators, whose connection weights coevolve along with the dynamical states of the phase oscillator in congruence with the Hebbian and anti-Hebbian adaptive rules, under the influence of external sinusoidal forcing to unravel the collective dynamical states due to a delicate balance between the former and the latter. In particular, the Hebbian adaptation mechanism for the connection weights was found to facilitate the manifestation of several interesting partially and completely synchronized states such as two-clusters, multiclusters, frequency-clusters, bump state, bump frequency clusters, forced entrained clusters, and forced entrained states. The anti-Hebbian adaptation mechanism for the coevolution of the connection weights and the dynamical states of the phase oscillators was found to facilitate the self-organization of itinerant chimera, characterized by time-dependent coexisting domains of coherent and incoherent dynamical states. The latter also resulted in the manifestation of an incoherent state, a multicluster state, and a forced entrained state. Further, we have introduced three distinct measures for the strength of incoherence based on the local standard deviations of the time-averaged frequency and the instantaneous phase of each oscillator, and time-averaged mean frequency for each bin to corroborate the distinct dynamical states and to demarcate the two parameter phase diagrams along with the Kuramoto order parameters. We have also deduced the existence and stability conditions for the forced entrained state, which is found to match very well with the simulation boundaries of the forced entrained state for both the Hebbian and anti-Hebbian mechanisms. We have also confirmed that the observed dynamical states and their transitions are robust in a range of

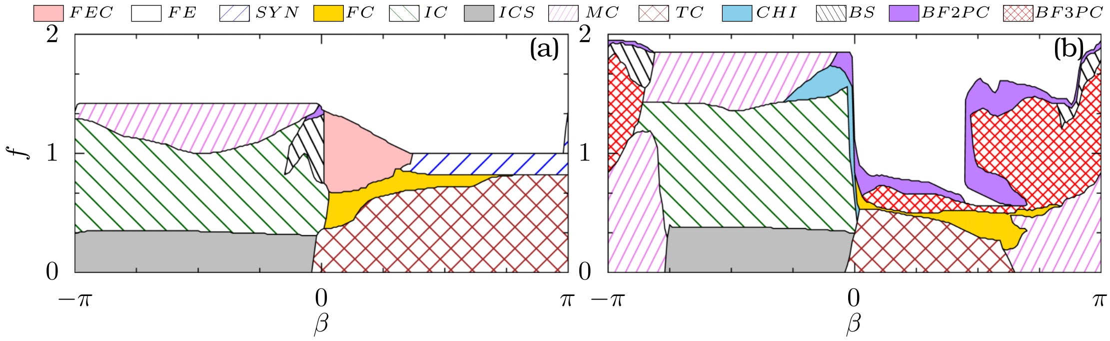

FIG. 17. The two-parameter phase diagram in the (β, f) parametric space for the phase-lag parameter (a) $\alpha = 0$ and (b) $\alpha = \pi/4$. The initial conditions for θ_i and k_{ij} are uniformly distributed in the interval $[0, 2\pi)$ and $(-1, 1)$ $\forall$ j, respectively. See the text for more explanations.

the natural frequency λ and for distinct initial conditions for k_{ij}.

It should be noted that since we have employed phase oscillators to investigate the emerging collective behaviors due to a delicate balance between the external forcing and the adaptation rules, the results are expected to be valid for any nonlinear oscillators, representing the variety of neuronal models, in the weak-coupling limit. However, the level of complexity and the specific adaptations considered may limit the direct generalization and applicability of our results to address the intricate patterns by the brain network despite the valuable insights into the behavior of adaptive networks of globally coupled oscillators. Our current work can be extended to understand how the external forcing (task) affects the adaptively coupled phase oscillator with feedback coupling weight in the adaptation rule. One can also extend the analysis for global and nonlocal interaction in adaptation rules. Furthermore, the impact of external forcing on the adaptively coupled multilayer networks is still an open problem.

ACKNOWLEDGMENTS

We acknowledge the pertinent comments of the anonymous referees, which helped us to improve the overall manuscript. The work of V.K.C. is supported by the DST - SERB - CRG Project under Grant No. CRG/2020/004353. The work of V.K.C. is also supported by DST, New Delhi for computational facilities under the DST-FIST programme (SR/FST/PS-1/2020/135) to the Department of Physics. The work of M.S. forms a part of a research project sponsored by the Science and Engineering Research Board, Government of India, under Grant No. CRG/2021/002428. D.V.S. is supported by the DST-SERB-CRG Project under Grant No. CRG/2021/000816.

---

[1] D. Taylor, E. Ott, and J. G. Restrepo, Phys. Rev. E **81**, 046214 (2010).
[2] J. Sawicki *et al.*, Chaos **33**, 071501 (2023).
[3] H. Markram, J. Lübke, and B. Sakmann, Science **275**, 213 (1997); L. F. Abbott and S. B. Nelson, Nat. Neurosci. **3**, 1178 (2000); H. Markram, J. Lübke, and B. Sakmann, N. Caporale and Y. Dan, Annu. Rev. Neurosci. **31**, 25 (2008).
[4] T. Gross, C. J. Dommar D'Lima, and B. Blasius, Phys. Rev. Lett. **96**, 208701 (2006); T. Gross and B. Blasius, J. R. Soc., Interface **5**, 259 (2008).
[5] S. Jain and S. Krishna, Proc. Natl. Acad. Sci. USA **98**, 543 (2001).
[6] L. Horstmeyer and C. Kuehn, Phys. Rev. E **101**, 022305 (2020).
[7] C. Kuehn, *Multiple Time Scale Dynamics* (Springer International, Switzerland, 2015).
[8] D. V. Kasatkin, S. Yanchuk, E. Schöll, and V. I. Nekorkin, Phys. Rev. E **96**, 062211 (2017).
[9] R. Berner, J. Sawicki, and E. Schöll, Phys. Rev. Lett. **124**, 088301 (2020).
[10] R. Gutiérrez, A. Amann, S. Assenza, J. Gómez-Gardeñes, V. Latora, and S. Boccaletti, Phys. Rev. Lett. **107**, 234103 (2011).
[11] E. Pitsik, V. Makarov, D. Kirsanov, N. Frolov, M. Goremyko, X. Li, Z. Wang, A. Hramov, and S. Boccaletti, New J. Phys. **20**, 075004 (2018).
[12] J. Fialkowski, S. Yanchuk, I. M. Sokolov, E. Schöll, G. A. Gottwald, and R. Berner, Phys. Rev. Lett. **130**, 067402 (2023).
[13] S. Thamizharasan, V. K. Chandrasekar, M. Senthilvelan, R. Berner, E. Schöll, and D. V. Senthilkumar, Phys. Rev. E **105**, 034312 (2022).
[14] A. D. Kachhvah and S. Jalan, New J. Phys. **24**, 052002 (2022).
[15] P. S. Skardal and A. Arenas, Phys. Rev. Lett. **122**, 248301 (2019).
[16] A. D. Kachhvah and S. Jalan, Phys. Rev. E **105**, L062203 (2022).
[17] S. N. Chowdhury, S. Rakshit, J. M. Buldu, D. Ghosh, and C. Hens, Phys. Rev. E **103**, 032310 (2021).
[18] R. G. M. Morris, D. O. Hebb, *The Organization of Behavior* (Wiley, New York, 1949).
[19] L. I. Zhang, H. W. Tao, C. E. Holt, W. A. Harris, and M. Poo, Nature (London) **395**, 37 (1998).
[20] G. Q. Bi and M. M. Poo, J. Neurosci. **18**, 10464 (1998).
[21] T. Aoki and T. Aoyagi, Phys. Rev. Lett. **102**, 034101 (2009); Phys. Rev. E **84**, 066109 (2011).
[22] C. B. Picallo and H. Riecke, Phys. Rev. E **83**, 036206 (2011).
[23] L. Timms and L. Q. English, Phys. Rev. E **89**, 032906 (2014).
[24] X. Zhang, S. Boccaletti, S. Guan, and Z. Liu, Phys. Rev. Lett. **114**, 038701 (2015).
[25] L. Lücken, O. V. Popovych, P. A. Tass, and S. Yanchuk, Phys. Rev. E **93**, 032210 (2016).
[26] S. Chakravartula, P. Indic, B. Sundaram, and T. Killingback, PLoS One **12**, e0178975 (2017).
[27] D. V. Kasatkin and V. I. Nekorkin, Radiophys. Quantum Electron **58**, 877 (2016); Chaos **28**, 093115 (2018); Eur. Phys. J.: Spec. Top. **227**, 1051 (2018).
[28] V. Avalos-Gaytán, J. A. Almendral, I. Leyva, F. Battiston, V. Nicosia, V. Latora, and S. Boccaletti, Phys. Rev. E **97**, 042301 (2018).
[29] M. H. Matheny *et al.*, Science **363**, eaav7932 (2019).
[30] V. Röhr, R. Berner, E. L. Lameu, O. V. Popovych, and S. Yanchuk, PLoS One **14**, e0225094 (2019).
[31] R. Berner, E. Schöll, and S. Yanchuk, SIAM J. Appl. Dyn. Syst. **18**, 2227 (2019).
[32] R. Berner, J. Fialkowski, D. V. Kasatkin, V. I. Nekorkin, S. Yanchuk, and E. Schöll, Chaos **29**, 103134 (2019).
[33] V. K. Chandrasekar, M. Manoranjani, and S. Gupta, Phys. Rev. E **102**, 012206 (2020).
[34] V. K. Chandrasekar, J. H. Sheeba, B. Subash, M. Lakshmanan, and J. Kurths, Physica D **267**, 36 (2014).
[35] C. Zhou, J. Kurths, and B. Hu, Phys. Rev. Lett. **87**, 098101 (2001).
[36] I. Z. Kiss, Y. Zhai, and J. L. Hudson, Science **296**, 1676 (2002).
[37] I. Z. Kiss, Y. Zhai, and J. L. Hudson, Phys. Rev. E **77**, 046204 (2008).
[38] M. Rusconi, A. Zaikin, N. Marwan, and J. Kurths, Phys. Rev. Lett. **100**, 128101 (2008).
[39] G. Pfurtscheller and C. Neuper, Neurosci. Lett. Suppl. **174**, 93 (1994); C. M. Krause, H. Lang, M. Laine, and B. Pörn, Electroencephalogr. Clin. Neurophysiol. **98**, 319 (1996); L. Leocani, C. Toro, P. Manganotti, P. Zhuang, and M. Hallet,

Electroencephalogr. Clin. Neurophysiology/Evoked Potentials Section **104**, 199 (1997).

[40] M. C. Moore-Ede, F. M. Sulzman, and C. A. Fuller, *The Clocks That Time Us* (Harvard University Press, Cambridge, 1982).

[41] J. C. Dunlap, J. J. Loros, and P. J. Decoursey, *Chronobiology: Biological Timekeeping* (Sinauer Associates, Massachusetts, 2003).

[42] R. G. Foster and L. Kreitzman, *Rhythms of Life: The Biological Clocks that Control the Daily Lives of Every Living Thing* (Yale University Press, New Haven, CT, 2005).

[43] P. Seliger, S. C. Young, and L. S. Tsimring, Phys. Rev. E **65**, 041906 (2002).

[44] T. Aoyagi and K. Kitano, Phys. Rev. E **55**, 7424 (1997).

[45] G. Ermentrout, J. Math. Biol. **12**, 327 (1981).

[46] E. E. Goldwyn and A. Hastings, J. Theor. Biol. **289**, 237 (2011).

[47] H. G. Schuster and P. Wagner, Biol. Cybern. **64**, 77 (1990).

[48] H. G. Schuster and P. Wagner, Biol. Cybern. **64**, 83 (1990).

[49] G. H. Paissan and D. H. Zanettee, Physica D: Nonlinear Phenom. **237**, 818 (2008).

[50] A. D. Kachhvah, X. Dai, and S. Jalan, New J. Phys. **22**, 122001 (2020).

[51] C. R. Laing and O. E. Omelćhenko, Chaos **30**, 043117 (2020).

[52] M. Owen, C. Laing, and S. Coombes, New J. Phys. **9**, 378 (2007).

[53] H. Schmidt and D. Avitabile, Chaos **30**, 033133 (2020).

[54] R. Gopal, V. K. Chandrasekar, A. Venkatesan, and M. Lakshmanan, Phys. Rev. E **89**, 052914 (2014).

[55] Note that one needs to be very careful about the choice of M as binning is known to cause biases in the analysis of observed data.

[56] Y. Kuramoto, *Chemical Oscillations, Waves and Turbulence* (Springer, New York, 1984).

[57] S. Shinomoto and Y. Kuramoto, Prog. Theor. Phys. **75**, 1105 (1986).

[58] O. E. Omel'chenko and M. Wolfrum, Phys. D: Nonlinear Phenom. **263**, 74 (2013).

[59] D. V. Kasatkin, V. V. Klinshov, and V. I. Nekorkin, Phys. Rev. E **99**, 022203 (2019).